

Tidally driven interannual variation in extreme sea level frequencies in the Gulf of Maine

H. E. Baranes¹, J. D. Woodruff¹, S. A. Talke², R. E. Kopp³, R. D. Ray⁴, and R. M. DeConto¹

¹Department of Geosciences, University of Massachusetts Amherst, Amherst, MA, USA, ²Civil and Environmental Engineering Department, California Polytechnic State University, San Luis Obispo, CA, USA, ³Department of Earth & Planetary Sciences and Institute of Earth, Ocean & Atmospheric Sciences, Rutgers University, New Brunswick, NJ, USA, ⁴Geodesy and Geophysics Laboratory, NASA Goddard Space Flight Center, Greenbelt, MD, USA

Corresponding author: Hannah Baranes (hbaranes@geo.umass.edu)

Key Points:

- We present a new quasi-nonstationary joint probability method that estimates tidally driven interannual fluctuations in flood hazard
- This method provides more precise and stable storm tide frequency estimates than extreme value distributions fit to measured storm tides
- In the Gulf of Maine, tides force decadal oscillations in the 1% annual chance storm tide at a rate exceeding mean historical sea-level rise

1 **Abstract**

2 Astronomical variations in tidal magnitude can strongly modulate the severity of coastal
3 flooding on daily, monthly, and interannual timescales. Here, we present a new quasi-
4 nonstationary skew surge joint probability method (qn-SSJPM) that estimates interannual
5 fluctuations in flood hazard caused by the 18.6 and quasi 4.4-year modulations of tides. We
6 demonstrate that qn-SSJPM-derived storm tide frequency estimates are more precise and stable
7 compared with the standard practice of fitting an extreme value distribution to measured storm
8 tides, which is often biased by the largest few events within the observational period. Applying
9 the qn-SSJPM in the Gulf of Maine, we find significant tidal forcing of winter storm season
10 flood hazard by the 18.6-year nodal cycle, whereas 4.4-year modulations and a secular trend in
11 tides are small compared to interannual variation and long-term trends in sea-level. The nodal
12 cycle forces decadal oscillations in the 1% annual chance storm tide at an average rate of ± 13.5
13 mm/y in Eastport, ME; ± 4.0 mm/y in Portland, ME; and ± 5.9 mm/y in Boston, MA. Currently
14 (in 2020), nodal forcing is counteracting the sea-level rise-induced increase in flood hazard;
15 however, in 2025, the nodal cycle will reach a minimum and then begin to accelerate flood
16 hazard increase as it moves toward its maximum phase over the subsequent decade. Along the
17 world’s meso-to-macro-tidal coastlines, it is therefore critical to consider both sea-level rise and
18 tidal non-stationarity in planning for the transition to chronic flooding that will be driven by sea-
19 level rise in many regions over the next century.

20 **Plain Language Summary**

21 Coastal management practices around flood risk often rely on estimates of the percent
22 chance of a particular flood height occurring within a year. For example, U.S. flood insurance
23 requires designating areas with a 100-year flood recurrence interval (the “100-year flood zone”).
24 When storms hit regions with large tides, the height and timing of high tide often determine
25 flood severity. Thus, the relationship between flood height and annual frequency can be altered
26 by natural, daily-to-decadal cyclical variation in tide heights. Here, we present a new method for
27 calculating annually-varying flood height–frequency relationships based on known tidal cycles.
28 Applying the new method in the Gulf of Maine, we find an 18.6-year-long tidal cycle (the *nodal*
29 *cycle*) has forced decadal variation in the 1% annual chance flood at a faster rate than the
30 historical average rate of sea-level rise over the past century. Currently, nodal cycle forcing is
31 counteracting the sea-level rise-induced increase in flood hazard; however, in 2025, the nodal
32 cycle will reach a minimum in the Gulf and then begin to accelerate flood hazard as it moves
33 toward its maximum over the subsequent decade. It is therefore critical to consider sea-level rise
34 and tidal variation in medium-term flood hazard planning.

35
36
37
38
39
40
41

42 **Glossary of acronyms**

43	GEV	Generalized Extreme Value distribution
44	GPD	Generalized Pareto distribution
45	GPD _{ST}	Generalized Pareto distribution fit to measured storm tides
46	JPM	Joint probability method
47	MSL	Mean sea level
48	NOAA	National Oceanic and Atmospheric Administration
49	qn-SSJPM	Quasi-nonstationary joint probability method
50	RJPM	Revised joint probability method
51	SLR	Sea-level rise
52	SSJPM	Skew surge joint probability method
53	ST _{0.01}	Storm tide at the 0.01 exceedances/year level

54 **1 Introduction**

55 Extreme coastal flooding poses a growing hazard to coastal communities (e.g. Hallegatte
56 et al., 2013; Neumann et al., 2015). Management practices around flood risk often require
57 estimates of extreme sea level recurrence intervals; for example, in the United States, federal
58 flood insurance and building codes depend on estimates of the current 100-year flood zone
59 (Galloway et al., 2006; Hunter, 2010; Buchanan et al., 2017). Coastal flood hazard, however, is
60 not stationary. The relationship between flood height and recurrence interval is approximately
61 log-linear, so even small interannual variations in storm surge, tides, waves, or mean sea-level
62 (trends on the order of millimeters per year) can significantly alter extreme sea level frequencies
63 (e.g. Oppenheimer et al., 2019). Robust statistical methods for considering sea-level non-
64 stationarity (Hunter, 2010; Buchanan et al., 2017; Wahl et al., 2017) have been used to
65 incorporate uncertain sea-level rise (SLR) projections into global (e.g. Lin et al., 2016; Garner et
66 al., 2017; Oppenheimer et al., 2019) and local (e.g. NYC, 2013; Douglas et al., 2016; Griggs et
67 al., 2017) hazard assessments. In this paper, we investigate the impact of quasi-deterministic
68 variation in astronomical tides on low-frequency, high-impact extreme sea levels.

69 Tidal magnitude modulates the severity of flooding in meso-to-macrotidal regions, and
70 interannual variation in tides causing periods of enhanced flood risk is a well-known
71 phenomenon (e.g. Sobey, 2005; Eliot, 2010; Menéndez & Woodworth, 2010; Ray & Foster,
72 2016; Talke et al., 2018; Peng et al., 2019; Haigh et al., 2020; Talke & Jay, 2020). In particular,
73 the 18.6-year lunar nodal cycle and the 8.85-year cycle of lunar perigee influence high water
74 globally on weekly, monthly, and annual timescales (e.g., Haigh et al., 2011; Peng et al., 2019).
75 Ray and Foster (2016) showed that the perigean cycle modulates predicted future nuisance tidal
76 flooding at a quasi 4.4-year period. For extreme flooding, Menéndez and Woodworth (2010)
77 modeled global nodal and perigean astronomical modulations using a non-stationary location
78 parameter in extreme sea level probability distributions fit to satellite altimetry records over the
79 1970–2008 time period. Over a longer, nearly 200-year record from Boston, Massachusetts,
80 Talke et al. (2018) also showed that the nodal cycle produces 10–20 cm of variation in extreme
81 sea levels with recurrence intervals between 2 and 100 years.

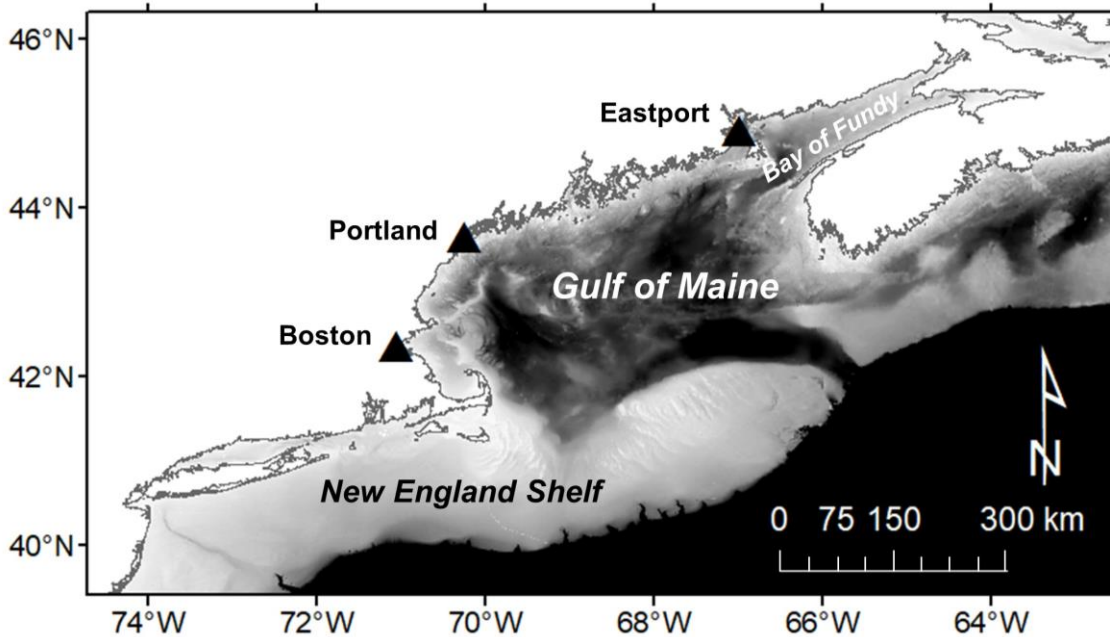
82 On decadal to centennial timescales, non-astronomical factors also force local-to-global-
83 scale variations and trends in tides (Schindelegger et al., 2018; Haigh et al., 2020; Talke & Jay,
84 2020). Changes in water depth, shoreline position, frictional resistance, and river flow have led
85 to dramatic local-scale tidal amplification and reduction over the past two centuries, particularly
86 in estuaries and tidal rivers (Winterwerp et al., 2013; Haigh et al., 2020; Talke & Jay, 2020).

87 Spatially coherent, regional-scale variation in tides has been driven by changes in ocean depth,
88 shoreline position, sea ice extent, ocean stratification, non-linear interactions, and radiational
89 forcing (e.g. Woodworth, 2010; Müller et al., 2011; Müller, 2012; Haigh et al., 2020).

90 In summary, interannual variations and long-term trends in tides have significant
91 implications for flood hazard. Astronomical nodal and perigean cycles can significantly increase
92 flood hazard compared to the long-term average during their positive phases (e.g. Talke et al.,
93 2018), and secular changes in tides driven by non-astronomical factors will either enhance or
94 counteract the increase in flood hazard driven by SLR (e.g. Haigh et al., 2020). Given that the
95 expected frequency of flooding changes year-to-year, considering sea-level rise and tidal non-
96 stationarity together is important to both short and long-term municipal planning and emergency
97 management at the coast. However, as mentioned by Talke et al. (2018), methods for assessing
98 tidally driven interannual variation in extreme sea-level hazard require further development.

99 In this paper, we describe a new method for estimating tidally driven non-stationarity in
100 extreme still water levels measured at tide gauges using an adaptation of the measurement-based
101 joint probability methods developed by Pugh and Vassie (1978, 1980), Tawn and Vassie (1989),
102 Tawn (1992), and Batstone et al. (2013). We apply and validate our methodology using century-
103 long tide gauge records from the Gulf of Maine coast in the northwest Atlantic Ocean (Fig. 1), a
104 region with significant nodal variability and secular trends in tides (Ray, 2006; Ray & Talke,
105 2019). Under the assumption of stationary storm characteristics, this new quasi-nonstationary
106 joint probability method provides separate statistical treatment of tides and surge and accounts
107 for interannual variation in tides. The we use the term “still water level” to convey that the tide
108 gauge-based analyses presented here do not consider wave impacts. Tide gauges located in
109 wave-sheltered harbors measure the contributions storm surge, tides, and mean sea level to flood
110 level (i.e. the still water level) but exclude waves (Melet et al., 2018; Dodet et al., 2019;
111 Woodworth et al., 2019). Note that in subsequent sections, we use the term “storm tides” for
112 extreme still water levels referenced to the annual mean sea-level.

113



114

115 **Figure 1.** Gulf of Maine site map, including gauge locations mentioned in the text.

116 2 Background

117 2.1 Site description

118 We apply this new quasi-nonstationary joint probability method to estimating extreme
119 still water level recurrence intervals at the three longest running and most complete National
120 Oceanic and Atmospheric Administration (NOAA) tide gauge records within the Gulf of Maine
121 at Boston, Portland, and Eastport (Fig. 1). Table 1 shows their locations, measurement
122 timespans, and relevant tidal datums. An additional record at St. John, New Brunswick (1893-
123 present) is not included because of significant data gaps and unusual interannual variation in the
124 amplitude of the M_2 tidal constituent after 1980 (Ray & Talke, 2019). In addition to its multiple
125 century-long tide gauge records, the Gulf of Maine's large tide range and known local and
126 regional tidal variation make it an ideal location for applying our statistical method. The region
127 also hosts major cities and sensitive infrastructure that require careful flood risk assessment; for
128 example, Hallegate et al. (2013) ranked Boston, Massachusetts within the top twenty cities
129 globally for modeled flood loss under both present-day and future (2050) scenarios.

130 The Gulf of Maine coast is vulnerable to flooding from both tropical and extratropical
131 cyclones, but extratropical cyclones have historically been the dominant flooding mechanism, as
132 they are more frequent and more likely to intersect with high tide due to their often longer
133 durations (e.g. Kirshen et al., 2008; Talke et al., 2018). The total still water level (i.e. not
134 including waves) recorded during a storm, relative to some vertical datum, is called *storm tide*
135 and represents the net impact of meteorological and tidal forcing. Here, we use annual mean sea
136 level (MSL) as the vertical datum, such that storm tide time series do not include SLR. *Storm*
137 *surge* is the meteorologically forced deviation from the predicted tide, calculated by subtracting
138 the predicted tide from time series of measured storm tide values. Extreme storm surges reach
139 ~1.3 meters in the Gulf (e.g. Talke et al., 2018), and tides are significantly larger. The great
140 diurnal tide range increases northward from 3.1 meters in Boston to ~16 meters in the Bay of
141 Fundy's northern embayments, making tides a primary control on most of the region's extreme
142 coastal flooding events. In Boston, for example, Talke et al. (2018) found that 92 of the top 100
143 storm events occurring between 1825 and 2018 coincided with a predicted high tide that
144 exceeded modern mean higher high water.

145 Tides in the Gulf of Maine and Bay of Fundy are unusual in several respects. In addition
146 to the well-known large tidal range, there is a natural resonance frequency in the Gulf near the
147 frequency of the N_2 tide (Garrett, 1972; Godin, 1993). Observed N_2 amplitudes are larger than S_2
148 amplitudes, although the opposite is true of the theoretical tidal potential; thus, the classic
149 fortnightly spring-neap modulation is relatively weak and is smaller than the monthly modulation
150 induced by M_2/N_2 beating. The strongest astronomical tides during any month therefore occur
151 near times of lunar perigee. Similar to many locations, there are additional modulations at
152 semiannual, 4.4-year, and 18.6-year periods (Haigh et al., 2011; Ray & Merrifield, 2019). The
153 4.4-year and 18.6-year modulations of the highest predicted tide are moderate at Boston and
154 Portland (roughly 3–4 cm in amplitude) but get much larger (up to 15 cm in amplitude) inside
155 the Bay of Fundy (Ray & Merrifield, 2019; see also Ray & Talke, 2019 for 18.6-year
156 modulations of the M_2 constituent in the Gulf of Maine). The 18.6-year modulation is caused by
157 the lunar nodal cycle, or a precession of the moon's orbital plane around the ecliptic 360° every
158 18.6 years. The 4.4-year modulation is caused by perigean spring tides coinciding with the
159 winter or summer solstice (when the diurnal tidal contribution is largest) twice per 8.85 years
160 (see Ray & Foster, 2016 for an explanation).

161 **Table 1.** Gulf of Maine NOAA tide gauge station info. The two right-most columns show winter and
 162 summer seasons omitted from the qn-SSJPM statistical analysis due to missing more than 25% of water
 163 level measurements. Two years are listed for each omitted winter season because we define the season as
 164 31 October through 30 April of the following year. Note that all records extend to the present, but we only
 165 use data through 2019 in our calculations.

Station; NOAA station no.	Approx. location	Mean higher high water (m) ^a	Great diurna l range (m) ^a	Timespan	Omitted winter seasons (< 75% complete)	Omitted summer seasons (< 75% complete)
Eastport, ME; 8410140	44°54.2'N 66°59.1' W	2.916	5.874	1929– 2019	1957/1958, 1962/1963, 1970/1971, 1971/1972, 1974/1975, 1975/1976, 1976/1977, 1977/1978, 1995/1996, 1998/1999	1929, 1957, 1958, 1963, 1971, 1974, 1976, 1978, 1980
Portland, ME; 8418150	43°39.3'N 70°14.8' W	1.513	3.019	1910– 2019	1910/1911, 1911/1912, 1933/1934, 1945/1946, 1960/1961	1910, 1911, 1956, 1961, 1970, 1971, 1990
Boston, MA; 8443970	42°21.2'N 71°3.0'W	1.545	3.131	1921– 2019	1944/1945	1921

166 ^a Tidal datums are relative to 1983-2001 mean sea level
 167

168 Perhaps owing to the basin resonance being near N_2 , Gulf of Maine tides are sensitive to
 169 small changes in basin geometry, depth, and friction. Indeed, they display some of the largest
 170 secular tidal trends observed anywhere in the world for a regional body of water. Since the early-
 171 20th century, the amplitude of the M_2 tidal constituent has steadily increased at an average rate of
 172 0.25 ± 0.04 mm/y at the Boston tide gauge, 0.59 ± 0.04 mm/y at Portland, and 0.77 ± 0.08 mm/y
 173 at Eastport (Ray & Talke, 2019). In comparison, average rates of SLR measured at these tide
 174 gauges over the same time period (see Tab. 1 for exact date range) are 2.83 ± 0.15 mm/y in
 175 Boston, 1.88 ± 0.14 mm/y in Portland, and 2.14 ± 0.17 mm/y in Eastport. New tide estimates
 176 derived from 19th-century water level measurements show that the M_2 trend began sometime in
 177 the late-19th or early-20th century, coincident with the transition to modern rates of SLR (Ray &
 178 Talke, 2019). Numerical models show that SLR has only caused part of the observed increase in
 179 M_2 amplitude in the Gulf of Maine (e.g. Müller et al., 2011; Greenberg et al., 2012; Pelling &
 180 Green, 2013; Schindelegger et al., 2018), suggesting that ocean stratification driven by sea-
 181 surface temperature warming has also played a role in the increase (Müller, 2012; Ray & Talke,
 182 2019).

183 2.2 Review of extreme sea level statistical methods

184 Extreme sea level recurrence intervals can be estimated from data or models. In both
 185 cases, an extreme value probability distribution is fit to a set of measured or simulated extreme
 186 sea levels assumed to be representative of the possible flood scenarios in a region.
 187 Hydrodynamic simulations have the advantage of explicitly including wave impacts and
 188 providing spatially continuous flood elevations and flow velocities; however, they are
 189 computationally intensive, take time to develop, and as with all models, rely on uncertain
 190 parameterizations, bathymetry, and assumptions (e.g. Vousdoukas et al., 2016; Lin et al., 2010).
 191 At gauged locations with multi-decadal records, estimating storm tide recurrence intervals from
 192 data is a simpler alternative that will be the focus of this paper.

193 The two most commonly used extreme value distributions are the Generalized Extreme
194 Value distribution (GEV) and the Generalized Pareto Distribution (GPD). The GEV is fit to
195 block maxima data, or the n-largest measurements per some time interval (e.g. the largest event
196 each year), and the GPD is fit to peaks-over-threshold data, or all measurements over some
197 threshold value that defines extremes. The GPD approach is more robust because it uses more
198 available extreme observations (e.g. NERC, 1975; Coles et al., 2001; Tebaldi et al., 2012;
199 Buchanan et al., 2017). In Boston, for example, only 46 of the top 100 storm tides recorded at the
200 NOAA gauge occurred in distinct years. A GEV using annual block maxima would therefore
201 omit more than half of the top-100 events. Compared with the GEV, however, the GPD requires
202 higher data quality and is more difficult to fit automatically because of its sensitivity to the
203 choice of threshold (Coles, 2001; Arns et al., 2013). Storm tide statistics published by NOAA,
204 for example, are derived from GEV fits because choosing a GPD threshold can be subjective,
205 and NOAA requires a method that can be quickly applied and periodically updated at over 100
206 gauges (Zervas, 2013). Nonetheless, Talke et al. (2018) found that GEV and GPD fits to Boston
207 extreme storm tides yielded similar recurrence interval estimates.

208 In meso-to-macrotidal regions, where tides are a primary control on flooding, a joint
209 probability approach that convolves separate tide and surge distributions can capture more
210 extreme storm surges within a temporally limited tide gauge record (e.g. Pugh & Vassie, 1979,
211 1980). For example, in 63 of the 100 years in Boston's record, the largest storm surge of the year
212 did not coincide with any of the year's top-3 storm tides; thus, a GPD fit to measured Boston
213 storm tides would exclude two-thirds of the largest storm surges (assuming a GPD threshold that
214 was exceeded, on average, three or fewer times per year). The first two published storm tide joint
215 probability methods were the Joint Probability Method (JPM; Pugh & Vassie, 1978, 1980) and
216 the Revised Joint Probability Method (RJPM; Tawn & Vassie, 1989; Tawn, 1992). The JPM
217 separates measured water levels into the predicted tide and a non-tidal residual (measured minus
218 predicted water level at a given time), fits an empirical probability distribution to each
219 component, and obtains the joint storm tide distribution by a convolution of the two component
220 distributions. The RJPM improves upon the JPM by 1) fitting a GEV distribution to extreme
221 non-tidal residual values in order to model events exceeding the observed maximum, and 2)
222 applying an extremal index that accounts for dependence of non-tidal residuals occurring close
223 together in time (the extremal index will be further explained in section 3.2).

224 The primary shortcoming of the JPM and RJPM is the assumed independence between
225 the predicted tide and the non-tidal residual. Storm surge and tides interact; storm surge increases
226 water depth, and tidal wave speed increases in deeper water (Horsburgh and Wilson, 2007). The
227 non-tidal residual time series of measured minus predicted water level therefore often includes
228 an "illusory" surge during storm events, which is an artifact of the difference in the predicted tide
229 and the phase-shifted tide. Furthermore, the amplitude, timing, and timescale of the surge wave
230 impacts its frictional interaction with tides (Famalkhalili et al., 2020).

231 The Skew Surge Joint Probability Method (SSJPM; Batstone et al., 2013) improves upon
232 the JPM by eliminating the bias introduced by the uncertain timing of the tidal prediction during
233 storm conditions. *Skew surge* is defined as the difference between the maximum measured water
234 level and the predicted high water within each tidal cycle. After accounting for seasonal variation
235 in tides, Williams et al. (2016) found statistical independence between predicted high water and
236 skew surge at 77 Atlantic tide gauges in the United States and Europe. They concluded that this
237 skew surge independence enables a simplified joint probability approach for calculating storm
238 tide recurrence intervals that does not require the inclusion of an empirical relationship between

239 tide and the non-tidal residual to account for tide-surge interaction. The argument is primarily
240 statistical and not dynamical, as the absence of correlation does not indicate the absence of
241 effect; rather, in observational records, natural variability in storm systems dominates over
242 tidally driven variation in surge. We address this issue by using primarily coastal (rather than
243 estuary) locations, such that frictional interaction effects are likely less prominent.

244 These joint probability methods have lowered bias in storm tide recurrence interval
245 estimates (compared to GPD or GEV fits to data) in regions where tides are large relative to
246 meteorological forcing, particularly for short data series (Dixon & Tawn, 1999; Haigh et al.,
247 2010); however, none has accounted for year-to-year fluctuations or secular trends in tidal
248 properties. In the following sections, we describe a new, quasi-nonstationary (*qn*) modification
249 of the SSJPM called the *qn*-SSJPM, which calculates a separate set of storm tide recurrence
250 intervals for winter and summer storm seasons using that season's known high tides. We fit
251 separate summer and winter distributions because the region's large storm events mostly occur in
252 the winter season (e.g. Talke et al., 2018), while summertime tide levels are larger on average
253 (Ray & Foster, 2016).

254 **3 Methods**

255 3.1 Tide gauge data processing

256 At the Eastport, Portland, and Boston NOAA gauges, we use hourly water level data
257 from NOAA, downloaded from the University of Hawaii Sea Level Center database for pre-2016
258 data (Caldwell et al., 2010) and from NOAA's website for post-2016 data
259 (<https://tidesandcurrents.noaa.gov>). We remove the annual MSL trend by subtracting a one-year
260 moving average of all hourly water level measurements (following Arns et al., 2013).

261 We fit a six-minute cubic spline function to the hourly data over the entire length of each
262 tide gauge record (six-minute data are only available from NOAA beginning in 1996) to reduce
263 the peak truncation caused by using hourly records. For example, hourly-based high waters from
264 Boston in 2018 were an average of 4.1 cm lower than 6-minute resolution records. The six-
265 minute spline fit reduces this bias to 0.7 cm. Since the precision of individual, pre-digital
266 measurements varies from 0.015 meters (due to rounding) to 0.05–0.1 meters or more during
267 periods with timing or gauge problems (e.g. Talke et al., 2018, 2020), this small bias is less than
268 other sources of error. All subsequent calculations use this MSL-adjusted six-minute spline fit to
269 the hourly data.

270 We estimate the tidal contribution to each water level measurement using the MATLAB-
271 based harmonic analysis program *r_t_tide* (Pawlowicz et al., 2002; Leffler and Jay, 2009). We
272 calculate tidal constituents independently for each year from a 369-day analysis that includes 67
273 constituents. The 369-day analysis enables estimation of the semiannual and annual constituents,
274 as well as the seasonal sidelines to M_2 (often called MA_2 and MB_2 , but mislabeled H_1 and H_2 in
275 *r_t_tide*). Since we are interested in the effect of the nodal cycle, no nodal corrections were
276 applied. *r_t_tide* also applies nodal corrections based on the astronomic potential, rather than the
277 empirically measured and slightly smaller correction observed in practice in the Gulf of Maine
278 (e.g. Ku et al., 1985; Ray & Foster 2016; Ray & Talke, 2019).

279 We calculate the skew surge parameter by subtracting maximum predicted water level
280 from maximum observed water level within each semidiurnal tidal cycle. Following Williams et
281 al. (2016), we test for statistical independence between predicted high water and the top 1% of
282 skew surge at all sites using the rank-based Kendall's Tau correlation test (Kendall, 1938), where

283 the criteria for significant correlation are $|\tau| > 0.1$ and $p < 0.05$. We do not find significant
 284 correlation between predicted high water and skew surge at any of the three sites (Tab. S1).

285 The final inputs into the joint probability analysis are semidiurnal predicted high waters
 286 (relative to annual MSL) and their associated skew surges over the length of each tide gauge
 287 record. Measured high waters are only used to calculate the declustering coefficient (see equation
 288 6 for calculating the extremal index in section 3.2). Prior to the joint probability analysis, we also
 289 divide tides and skew surges into the winter storm season, defined as 31 October to 30 April, and
 290 the more quiescent summer season, defined as 1 May to 30 October (Wahl and Chambers, 2015;
 291 Thompson et al., 2013). Including 31 October in the winter storm season avoids exclusion of a
 292 1991 hybrid storm (Talke et al., 2018). In all subsequent analyses, we only include seasons
 293 where the set of measured water levels is at least 75% complete (Menéndez and Woodworth,
 294 2010; Wahl and Chambers, 2015). Table 1 lists the winter and summer seasons omitted at each
 295 tide gauge.

296 3.2 Quasi-nonstationary joint probability analysis (qn-SSJPM)

297 We calculate storm tide exceedance curves for each season, where the expected number
 298 of exceedances (i.e. the number of storm tides exceeding a certain level) is equal to the inverse of
 299 recurrence interval. Each winter or summer-season storm tide exceedance curve is calculated by
 300 convolving probability distributions of that season's predicted high waters and all winter or
 301 summer skew surges recorded over the length of the tide gauge record. We model winter and
 302 summer extreme skew surge probabilities with a GPD following Batstone et al. (2013). For skew
 303 surges x above a threshold μ , the GPD cumulative distribution function $G_{SS}(x)$ takes the form

$$304 \quad G_{SS}(x) = 1 - \left(1 + \xi \frac{x - \mu}{\sigma}\right)^{-1/\xi} \quad (1)$$

305 with shape parameter $\xi \neq 0$ and scale parameter $\sigma > 0$. To account for uncertainty in the skew
 306 surge GPD, we sample 1,000 pairs of ξ and σ from the covariance matrix of their maximum
 307 likelihood estimates with Latin hypercube sampling (Buchanan et al., 2016, 2017). We choose
 308 the GPD threshold that defines extreme skew surges by minimizing the root mean square error of
 309 GPD exceedances versus empirically-derived storm tide plotting positions (Arns et al., 2013).
 310 We calculate plotting positions using the Weibull formula

$$311 \quad \tilde{F}_{SS}(x_i) = \frac{i}{n+1} \quad (2)$$

312 where x_i is the i th-largest skew surge, and n is the total number of skew surges. We find that
 313 setting the threshold as the 99.7th percentile of skew surges for both the winter and summer
 314 seasons minimizes error across all sites, and past studies have used a similarly high threshold
 315 (Menéndez and Woodworth, 2010; Arns et al., 2013). This 99.7th percentile threshold samples an
 316 average of 1.1 events per season. Following Batstone et al. (2013), we assume there are
 317 sufficient observations to use the empirical distribution $\tilde{F}_{SS}(x)$ (i.e. plotting positions; equation 2)
 318 for skew surges below the threshold, such that the cumulative distribution function of all skew
 319 surges $F_{SS}(x)$ is

$$320 \quad F_{SS}(x) = \begin{cases} \tilde{F}_{SS}(x), & x < \mu \\ (1 - 0.997) * G_{SS}(x) + 0.997, & x \geq \mu \end{cases} \quad (3)$$

321 We then calculate the joint cumulative distribution function of storm tides $F_{ST}(z)$ for
 322 each season following the SSJPM (Batstone et al., 2013), which assumes that there is an equal
 323 probability of a given skew surge occurring at any high tide in a season:

$$324 \quad F_{ST}(z) = \left[\prod_{t=1}^{N_{HW}} F_{SS}(z - P_t) \right]^{1/N_{HW}} \quad (4)$$

325 where z is storm tide, P_t is the predicted high water in tidal cycle t , and N_{HW} is the total number
 326 of high waters in the season. To account for statistical uncertainty in the skew surge GPD
 327 parameters, tides are convolved with all 1,000 skew surge GPDs (F_{SS}). The 50th quantile of the
 328 resulting 1,000 storm tide distributions (F_{ST}) represents the central estimate, and the 5th and 95th
 329 quantiles provide a 90% uncertainty range. We convert storm tide cumulative probabilities to
 330 expected number of exceedances per season $N(z)$ by

$$331 \quad N(z) = [N_{HW} * \theta(z)] * [1 - F_{ST}(z)] \quad (5)$$

332 where $\theta(z)$ is the extremal index, which effectively reduces the number of high waters per
 333 season to the number of independent high waters per season to account for events that span
 334 multiple high tides (Leadbetter, 1983; Tawn, 1992). The extremal index is the inverse of mean
 335 cluster size (the mean number of storm tides exceeding a certain height that are associated with a
 336 single event) and calculated as a function of storm tide, following Ferro and Segers (2003):

$$337 \quad \frac{1}{\theta(z)} = \frac{2 \left[\sum_{i=1}^{E(z)-1} (I(z)_i - 1) \right]^2}{(E(z) - 1) * \sum_i^{E(z)-1} [(I(z)_i - 1) * (I(z)_i - 2)]} \quad (6)$$

338 where $E(z)$ is the number of measured storm tides exceeding z , and $I(z)$ is interexceedance time.
 339 We find that the extremal index reduces storm tide magnitudes in the 1 to 30-year recurrence
 340 interval range; thus, it is likely that these water levels are sometimes exceeded multiple times
 341 during a single storm event, while the most extreme water levels with recurrence intervals longer
 342 than 30 years are generally independent.

343 At each site, the final products of the qn-SSJPM calculations include:

- 344 1. A storm tide exceedance curve for each summer and winter season in the NOAA record
- 345 2. Full-year (i.e. combined winter and summer) storm tide exceedance curves for each year
 346 in the NOAA record, calculated by adding the expected number of summer and winter
 347 exceedances in a given year for each storm tide height
- 348 3. Two time-integrated storm tide exceedance curves (one winter, one summer), calculated
 349 using winter or summer tides over the full length of the NOAA record
- 350 4. One full-year, time-integrated storm tide exceedance curve

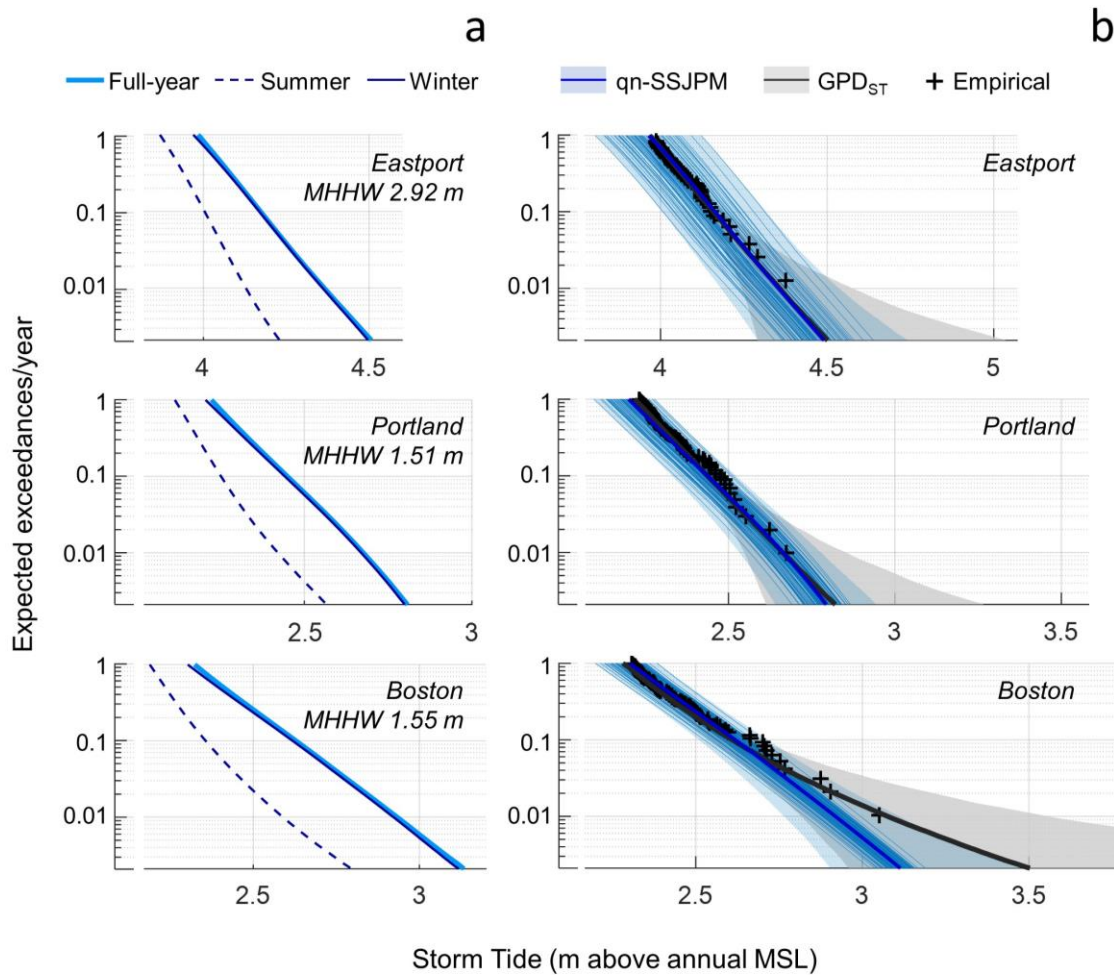
351 **4 Results and discussion**

352 4.1 qn-SSJPM results

353 We focus our discussion on winter storm season results because extreme flooding is
 354 primarily a winter hazard in the Gulf of Maine. A comparison of the time-integrated qn-SSJPM
 355 storm tide exceedance curves for winter, summer, and the full year (Fig. 2a) shows that storm
 356 tides from the full-year curves are, at most, 1.5 cm higher than winter curves at frequencies

357 below 0.1 expected exceedances/year. Thus, when viewing the full-year curve, it is important to
 358 do so with the caveat that summer floods are only a minor contributor to total flood hazard.

359 Figure 2b shows the winter-season annual and time-integrated storm tide exceedance
 360 curves for Eastport, Portland, and Boston. The spread among annual curves represents
 361 deterministic tidal variability and is thus greatest in Eastport where tide range and nodal cycle
 362 amplitude are the largest. As an example, the winter storm tide with 0.01 expected
 363 exceedances/year ranges 4.20–4.50 meters in Eastport, 2.56–2.74 meters in Portland, and 2.83–
 364 2.99 meters in Boston depending on the tidal properties of the calendar year (note that all storm
 365 tides are relative to annual MSL). The 90% uncertainty region (blue shading in Fig. 2b)
 366 encompasses both deterministic tidal variability and statistical uncertainty in the skew surge
 367 GPD parameters.



368
 369 **Figure 2.** Gulf of Maine storm tide exceedance curves. (a) Seasonality of flood hazard. Historical time-
 370 integrated qn-SSJPM storm tide exceedance curves are compared for the full year (thick solid line),
 371 summer season (dashed line), and winter season (thin solid line). (b) Comparison of winter-season storm
 372 tide exceedance curves for the qn-SSJPM and a GPD fit to measured storm tides (GPD_{ST}). Thin blue
 373 curves show qn-SSJPM-derived curves for each winter storm season in the tide gauge record, and bold
 374 blue curves are the time-integrated qn-SSJPM curves based on the entire tide gauge record. Black curves
 375 are a GPD_{ST} fit to the top 0.3% of storm tides in each tide gauge record, and + signs are empirical
 376 exceedances (see equation 2). Lines represent central estimates (50th quantile), and filled regions show the
 377 90% uncertainty range (5th–95th quantiles) for each method.

378 We also compare qn-SSJPM storm tide exceedance distributions to a GPD fit to the top
379 0.3% of storm tides in each record (Fig. 2b). This is a common approach for deriving storm tide
380 exceedances (see section 2.2), hereafter referred to as GPD_{ST} . We fit GPD_{ST} following the same
381 methods described in section 3.2 for fitting the skew surge GPD, using the 99.7th percentile of
382 measured storm tides as the GPD threshold. Uncertainty ranges are larger for the GPD_{ST}
383 distributions than the qn-SSJPM distributions (gray versus blue shaded regions in Fig. 2b).
384 Although both incorporate GPD parameter uncertainty, for the qn-SSJPM, the deterministic
385 predicted high water distribution reduces overall uncertainty. In Boston, the GPD_{ST} method
386 estimates significantly higher winter storm tides at exceedance levels < 0.1 compared to the qn-
387 SSJPM. Given the disagreement, we 1) use Monte Carlo simulations to validate the two
388 statistical approaches, 2) compare the Boston qn-SSJPM and GPD_{ST} exceedance curves to a
389 GPD_{ST} exceedance curve fit to an extended, 200-year long record of Boston storm tides (Talke et
390 al., 2018), and 3) test for sensitivity to GPD threshold selection for in each method.

391 4.2 Monte Carlo validation

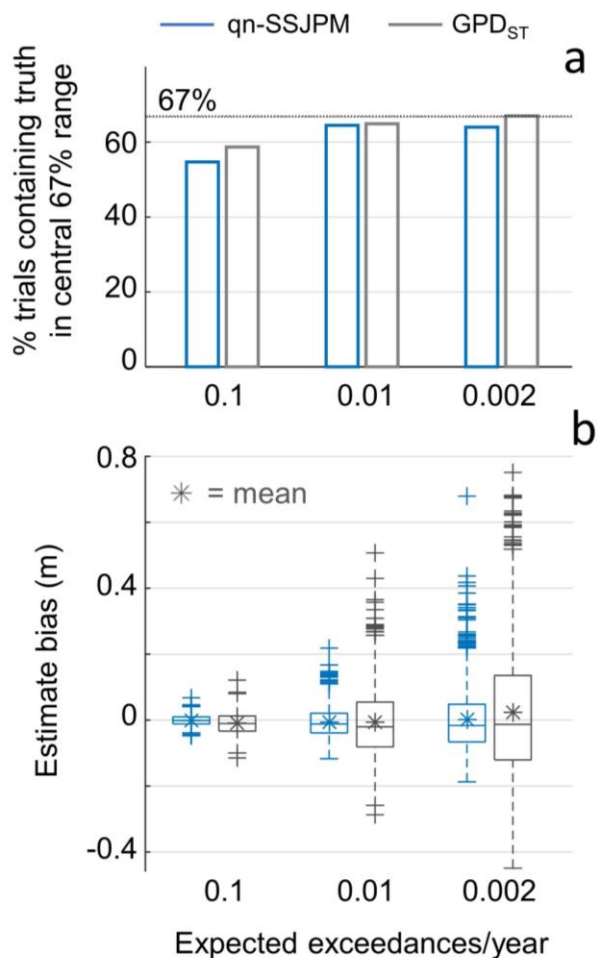
392 We compare the validity of the qn-SSJPM and GPD_{ST} methods using Monte Carlo
393 simulations. We create a synthetic 10,000-year time series of winter-season high waters by
394 splicing together the 1921–2018 Boston winter-season predicted high waters 102 times (102
395 times the 98-year record $\approx 10,000$ years) and combining each predicted high water with a skew
396 surge randomly sampled from the cumulative distribution function of Boston winter skew surges.
397 We treat empirical storm tide exceedances calculated from the synthetic 10,000-year record
398 (equation 2) as the “truth.” We then run 1,000 trials of randomly selecting 100 of the 10,000
399 years and calculating storm tide exceedance distributions based on those 100 years using both the
400 qn-SSJPM and GPD_{ST} methods. We use the 99.7th percentile storm tide and skew surge as GPD
401 thresholds, and for the qn-SSJPM calculation, we only generate a single time-integrated storm
402 tide exceedance distribution for the 100 years (i.e. we do not calculate annual distributions).
403 These simulations test how reliably the two statistical methods can represent flooding conditions
404 over 10,000 years based on a limited “observational” period of 100 years.

405 In analyzing the results, “estimate” refers to the storm tide-exceedance relationship
406 calculated from a 100-year subsample using the qn-SSJPM or GPD_{ST} methods. “Truth” refers to
407 the empirical storm tide-exceedance relationship calculated from the synthetic 10,000-year
408 record. For each of the 1,000 trials, we determine 1) whether or not the truth falls within the
409 central 67% ranges of storm tide estimates at the 0.1, 0.01, and 0.002 exceedances/year levels for
410 the two methods, and 2) the bias of the estimates, calculated as the difference between the truth
411 and the central (50th quantile) qn-SSJPM and GPD_{ST} storm tide estimates at the 0.1, 0.01, and
412 0.002 exceedances/year levels.

413 We find that the truth falls within the central 67% range of estimates 55–65% of the time
414 for the qn-SSJPM and 59–67% of the time for GPD_{ST} (Fig. 3a). Both methods’ overlap with the
415 truth generally increases at lower exceedance levels because uncertainty range also increases
416 with decreasing expected exceedances. The lower coverage of qn-SSJPM error ranges indicates
417 that the method’s estimate errors are more overconfident than GPD_{ST} estimate errors; however,
418 both the qn-SSJPM and GPD_{ST} have reasonable coverage.

419 Comparing biases in qn-SSJPM and GPD_{ST} estimates of storm tides at the 0.1, 0.01, and
420 0.002 exceedances/year levels reveals that qn-SSJPM estimates are more precise and stable (i.e.
421 consistently closer to the truth). Box plots in Figure 3b show each method’s biases for all 1,000
422 trials. The interquartile ranges increasing (i.e. the boxes getting larger) at lower exceedance

423 levels reflects the expected trend of increasing instability (i.e. variability) in estimated
 424 exceedances at lower exceedance levels for a given record length (e.g. Haigh et al., 2010). Mean
 425 bias is close to zero for both methods at all three exceedance levels; however, for storm tides at
 426 the 0.01 and 0.002 exceedances/year levels, both the interquartile range and total range in biases
 427 are significantly narrower for qn-SSJPM estimates than for GPD_{ST} estimates. This result
 428 indicates that for a 100-year observational record, both methods will, on average, provide
 429 accurate storm tide estimates between the 0.1 and 0.002 exceedances/year levels; however,
 430 GPD_{ST} estimates of storm tides with recurrence intervals nearing the record length (e.g. the storm
 431 tide with a 100-year recurrence interval or 0.01 expected exceedances/year for a 100-year-long
 432 record), are more susceptible to being biased by the largest few events within the observational
 433 period. This finding is consistent with past studies that have shown GPD and GEV fits to
 434 observed storm tides (often called “direct methods” of estimation) are more unstable to historical
 435 outlier events than joint probability distributions that incorporate large historical storm surges not
 436 necessarily coinciding with high tides (e.g. Tawn and Vassie, 1989; Tawn, 1992; Haigh et al.,
 437 2010).



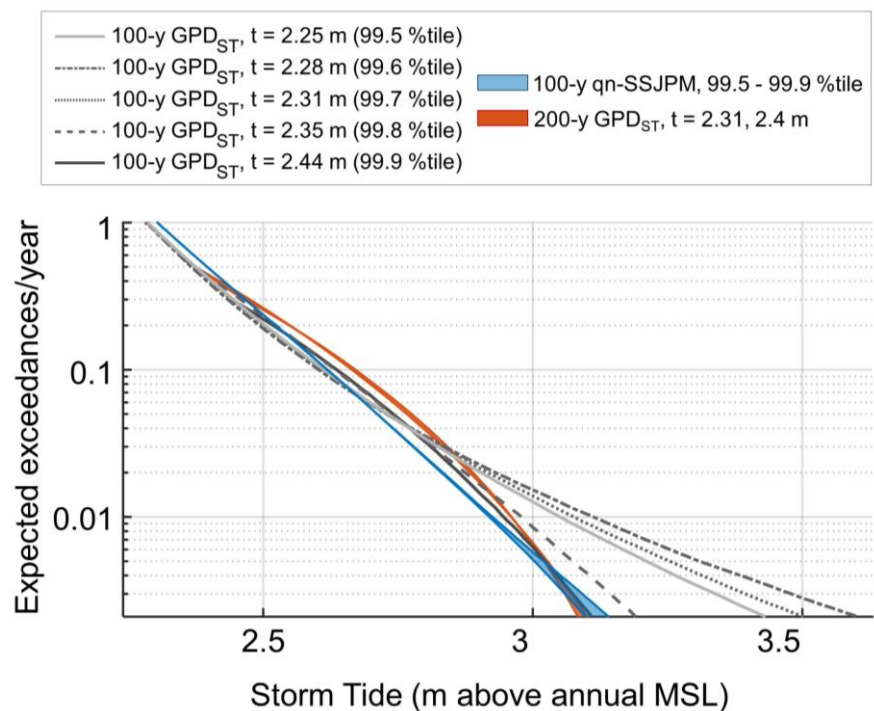
439 **Figure 3.** Validation results. (a) Percent of
 440 the 1,000 validation trials that contain the
 441 truth (empirical value) within the central
 442 67% range of storm tide estimates at the 0.1,
 443 0.01, and 0.002 exceedances/year levels for
 444 the qn-SSJPM method (blue) and the GPD_{ST}
 445 method (gray). (b) Box plot showing the
 446 distribution of qn-SSJPM and GPD_{ST} biases
 447 for the 1,000 validation trials at the 0.1, 0.01,
 448 and 0.002 exceedances/year levels. Biases
 449 are calculated as the difference between the
 450 truth (based on the empirical distribution
 451 calculated from the 10,000-year synthetic
 452 record) and the central qn-SSJPM estimates
 453 (blue) or GPD_{ST} estimates (gray). Central
 454 marker is the median (with the * symbol
 455 showing the mean), and bottom and top box
 456 edges are the 25th and 75th quartiles. Values
 457 plotted as outliers (+ markers) fall outside the
 458 central 99.3% range.

438
 439
 440
 441
 442
 443
 444
 445
 446
 447
 448
 449
 450
 451
 452
 453
 454
 455
 456
 457
 458

This instability to historical outliers partially explains the disagreement between the qn-SSJPM and GPD_{ST} curves for Boston (Fig. 2b). Boston’s highest three recorded flood events all occurred in years with unusually large tides (Talke et al., 2018). For example, the Blizzard of 1978 (the storm tide of record), happened to coincide with the year that, on average, had the

464 largest-magnitude high waters over the past century (represented by the right-most blue curve in
 465 Fig. 2b and highlighted with a red arrow in Fig. 5). Thus, the GPD_{ST} method in part
 466 overestimates Boston flood hazard because it does not account the Blizzard of 1978's 3.05-meter
 467 flood having had a lower probability of occurrence during any of the other 97 winters of record.

468 4.3 Extended Boston record and GPD threshold sensitivity



469
 470 **Figure 4.** Sensitivity of Boston winter storm tide exceedance curves to GPD threshold selection and
 471 comparison to the extended, 200-year Talke et al. (2018) record. The five gray storm tide exceedance
 472 curves are calculated using a GPD fit to measure storm tides in the 100-year NOAA record (GPD_{ST}
 473 method) with the threshold set as the 99.5th, 99.6th, 99.7th, 99.8th, and 99.9th percentile of measured storm
 474 tides. The red shaded region shows GPD_{ST} exceedance curves fit to the 200-year Talke et al. (2018)
 475 record using a 2.31-meter threshold (same as Fig. 2b) and a 2.4-meter threshold (value used by Talke et
 476 al.). The blue shaded region shows five qn-SSJPM exceedance curves fit to the 100-year NOAA record,
 477 with the skew surge GPD threshold set as the same five percentiles of skew surges (99.5th–99.9th
 478 percentiles).

479
 480 Comparing the Boston qn-SSJPM and GPD_{ST} winter storm tide exceedance curves (Fig.
 481 2b) to exceedance curves fit to the Talke et al. (2018) extended 200-year storm tide record also
 482 highlights the stability of the qn-SSJPM relative to the GPD_{ST} method. Gray curves in Figure 4
 483 show five GPD_{ST} fits to the 1921–2018 NOAA record using five different GPD thresholds,
 484 ranging 2.25 to 2.44 meters (the 99.5th to 99.9th percentiles of measured winter storm tides; Tab.
 485 S2). For the 100-year NOAA record, the five exceedance curves begin to diverge below the 0.03
 486 exceedances/year level, demonstrating the sensitivity of the GPD_{ST} method to threshold
 487 selection. The red shaded region in Figure 4 shows GPD_{ST} curves fit to the extended 1825–2018
 488 Boston record (un-bias corrected Data Set S3 from Talke et al., 2018) using both a 2.40-meter
 489 threshold (the value used by Talke et al., 2018) and a 2.31-meter threshold (the value used in Fig.
 490 2b that provides the best match to empirical exceedances). In contrast to the NOAA-record

491 curves, the narrowness of the red shaded region indicates that the longer, 200-year dataset makes
492 the GPD_{ST} method stable down through the 0.002 exceedances/year level.

493 The blue shaded region in Figure 4 shows the qn-SSJPM fit to the NOAA record using
494 five different thresholds for the GPD fit to skew surges (99.5th through 99.9th percentiles; Tab.
495 S2). The small variability among the five curves (i.e. the narrowness of the blue shaded region)
496 shows that with the shorter NOAA record, the qn-SSJPM can achieve the same stability with
497 respect to GPD threshold selection as the GPD_{ST} fit to the 200-year record. Finally, the
498 agreement at low exceedance levels between the qn-SSJPM and 200-year exceedance curves is
499 further evidence that the qn-SSJPM provides a more reliable characterization of extreme storm
500 tide frequencies than the GPD_{ST} method based on the 100-year NOAA record.

501 4.4 Interannual variation in storm tide frequency

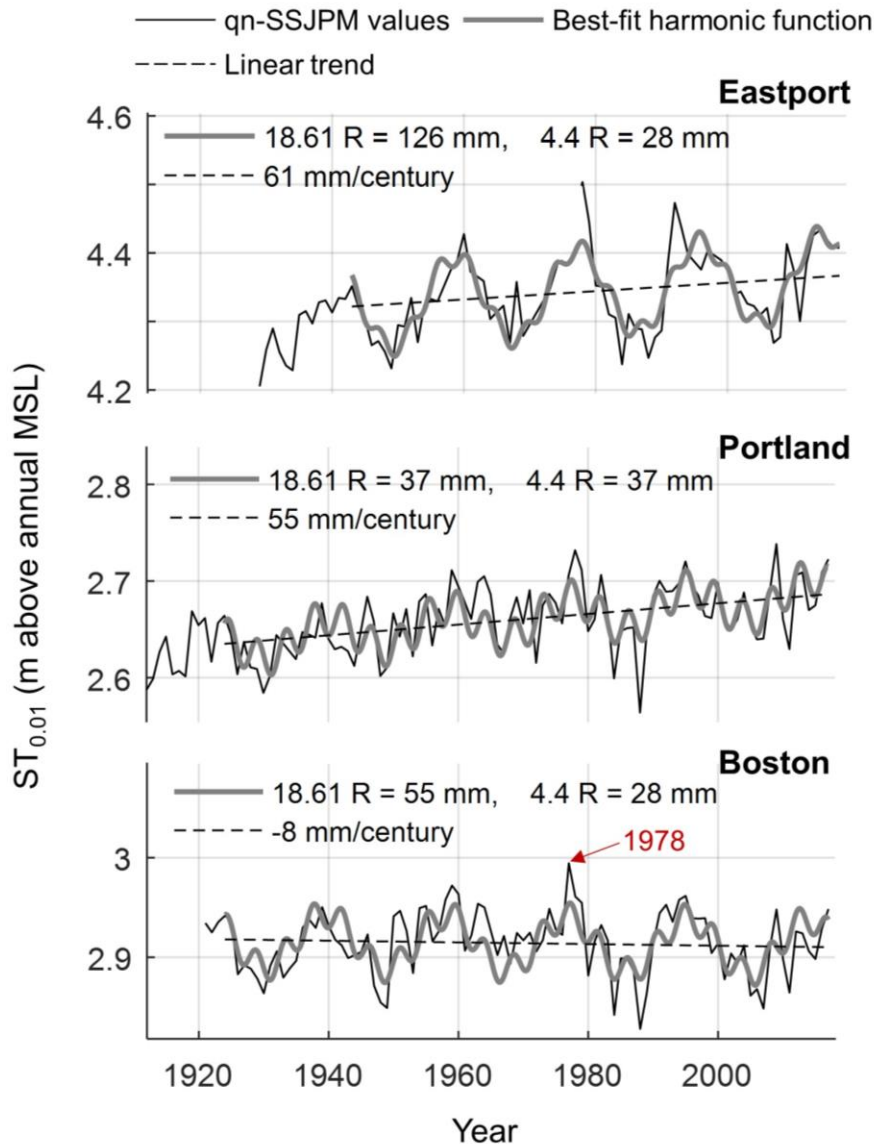
502 Interannual variation in tides forces changes in flood hazard on annual-to-decadal
503 timescales that should be considered in coastal management practices tied to storm tide
504 frequency estimates. We quantify the tidal modulation of flood hazard over the past century in
505 Eastport, Portland, and Boston using the annual time series of winter storm season storm tides at
506 the 0.01 exceedances/year level (hereafter referred to as $ST_{0.01}$) taken from the qn-SSJPM curves
507 (Fig. 5). To represent the three dominant sources of interannual tidal variability in the region (see
508 Ray & Foster, 2016), we fit a harmonic function to the time series with an 18.6-year period, a
509 4.4-year period, and a linear trend, where $ST_{0.01}$ values are relative to annual MSL, so the linear
510 trend is the increase in tides above SLR. The ranges (twice the amplitudes) of the 18.6 and 4.4-
511 year harmonics represent the magnitudes of the tidal cycles' forcing of flood hazard.

512 Table 2 compares 18.6 and 4.4-year modulations of $ST_{0.01}$ and of the highest predicted
513 tide (the highest tide in a 6-month interval), which are computed directly from harmonic
514 constants at the gauges. The 18.6 and 4.4-year cycles' forcing of $ST_{0.01}$ is perhaps smaller than
515 that of the highest predicted tide because $ST_{1\%}$ is calculated from observations rather than
516 predictions. Observed water level data include atmospheric effects, which introduce variability
517 that could interfere with tidal modulations. The exclusion of summer-season tides in the winter
518 $ST_{0.01}$ values also likely reduces 4.4-year periodicity in predicted water levels (e.g. Talke et al.,
519 2018). Finally, Peng et al. (2019) showed that the 18.6-year modulation of tides is greater for
520 more extreme high waters (for example, the modulation of monthly maximum high waters is
521 greater than that of monthly 99th percentile high waters). Similarly, modulation of $ST_{0.01}$
522 potentially reflects less extreme tidal levels than what would be obtained using the 6-month
523 maximum.

524 The secular increase in tides observed in the M_2 tidal constituent (e.g. Ray & Talke,
525 2019) has driven roughly a 0.6 mm/y increase in $ST_{0.01}$ in Eastport and Portland. In Boston,
526 however, there is a slight negative linear trend in $ST_{0.01}$ of -0.08 mm/y. Thus, the increase in tides
527 has had a minimal decadal-timescale impact on $ST_{0.01}$ compared to other forcings; however, in
528 Eastport and Portland, the total secular increase in $ST_{0.01}$ over the length of the tide gauge record
529 is comparable to decadal nodal variability. There is likely to be a future increase in high water
530 levels with SLR (Greenburg et al., 2012; Pelling & Green, 2013; Schindelegger et al., 2018) and
531 increasing tidal range (Greenberg et al., 2012), but there are no detailed projections for Gulf of
532 Maine tides that consider additional forcing mechanisms, such as changes in stratification and
533 flooding (Haigh et al., 2020).

534 The significance of the 4.4 and 18.6-year tidal modulations of $ST_{0.01}$ can best be
535 illustrated by converting the tidal cycle forcing ranges to rates and comparing them to rates of

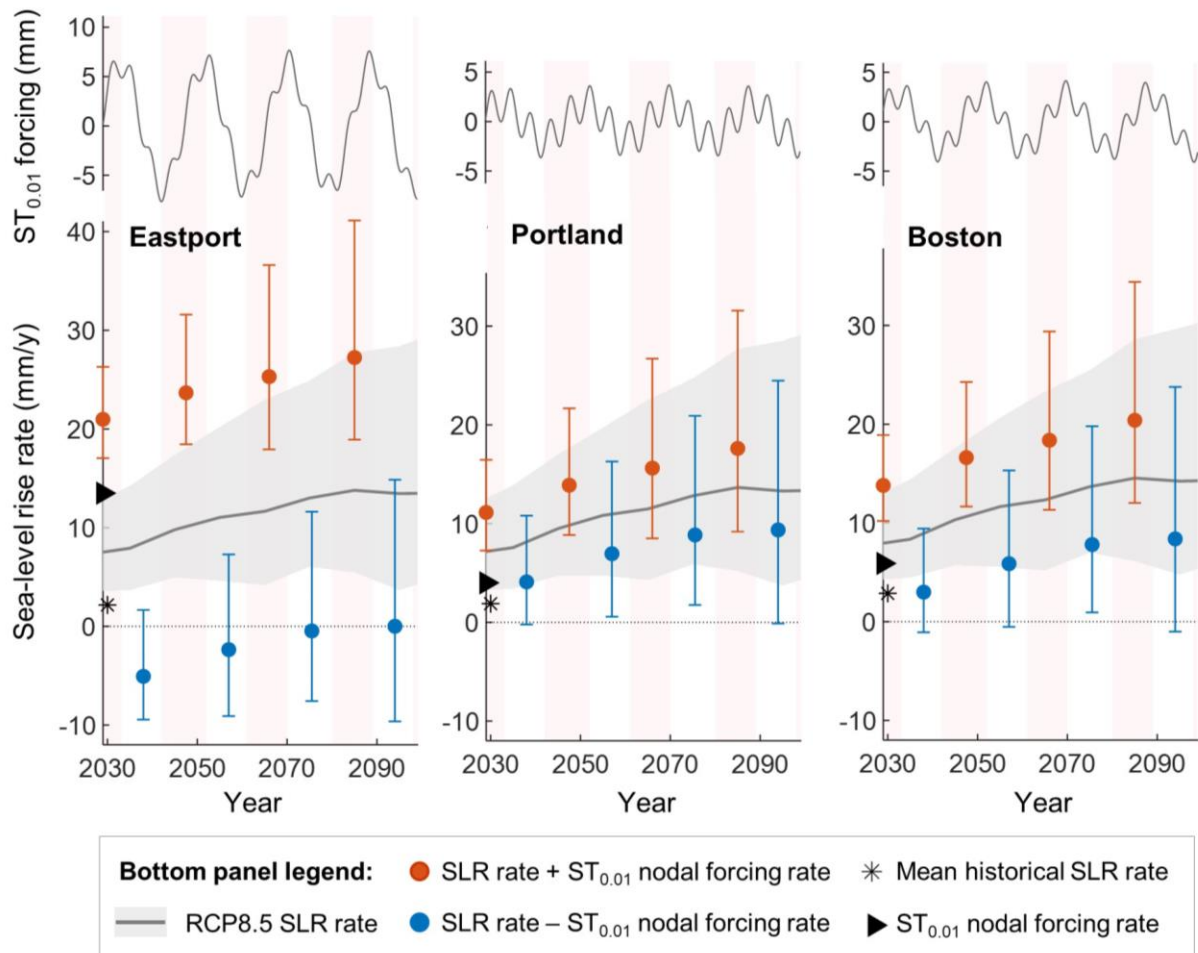
536 SLR. In Eastport, for example, the average range in 18.6-year forcing of $ST_{0.01}$ is 126 mm (Fig.
 537 5). The 18.6-year forcing can be positive or negative, so over any half nodal period in Eastport,
 538 the average rate of nodal forcing of $ST_{0.01}$ is ± 126 mm per 9.3 years, or ± 13.5 mm/year. Applying
 539 the same calculation to Portland and Boston, the average 18.6-year tidal forcing rates are ± 4.0
 540 mm/year and ± 5.9 mm/year, respectively. 4.4-year tidal forcing rates are a slower ± 3.0 mm/year
 541 in Eastport and Boston and ± 4.0 mm/year in Portland. In practice, however, interannual variation
 542 in winter MSL (which has historically been on the order of tens of mm) would drown out this
 543 shorter-period 4.4-year tidal modulation.



544 **Figure 5.** Interannual variation in the winter storm tides at the 0.01 exceedances/year level ($ST_{0.01}$). Time
 545 series of qn-SSJPM-derived annual $ST_{0.01}$ values (black line) with a least squares best-fit harmonic
 546 function that represents the region's dominant tidal forcings (gray curve), which includes an 18.6-year
 547 period, a 4.4-year period, and a linear trend. Legends show the ranges (i.e. double the amplitude) of the
 548 best-fit sinusoids and the slopes of the linear trends. Note the gap in the Eastport $ST_{0.01}$ time series where
 549 winter seasons were omitted due to less than 75% data completeness (see Tab. 1).
 550

552 **Table 2.** Ranges of 18.6 and 4.4-year tidal cycle modulations of the storm tides at the 0.01
 553 exceedances/year level ($ST_{0.01}$) and the highest predicted tide.

	18.6-year modulation range (mm)		Quasi 4.4-year modulation range (mm)	
	$ST_{0.01}$	Highest predicted tide	$ST_{0.01}$	Highest predicted tide
Eastport	126	196	28	78
Portland	37	66	37	68
Boston	55	72	28	62



554

555 **Figure 6.** Joint impact of tidal forcing and sea-level rise on future flood hazard increase. (Top panel) 18.6
 556 and 4.4-year components of the best-fit harmonic function to the winter $ST_{0.01}$ time series from Fig. 5.
 557 (Bottom panel) Gray curves show projected rates of local RCP8.5 SLR modified from Kopp et al. (2014)
 558 (line = 50th quantile of samples, shading = central 90% range). Over 9.3-year-intervals where the nodal
 559 cycle is moving from a minimum to a maximum (indicated by red shading), the average nodal forcing rate
 560 (black triangle on y-axis) is added to the average projected rate of SLR over the same 9.3 years (red
 561 circles, with bars representing SLR uncertainty). Over intervals when the nodal cycle is trending
 562 negatively, nodal forcing is subtracted from the rate of SLR (blue circles and bars). The historical rate of
 563 SLR over the past century is also shown for reference (black asterisk on the y-axis).

564 Figure 6 provides a visualization of the impact of 18.6-year forcing in the context of
565 SLR. On decadal timescales, the natural variability in $ST_{0.01}$ (and therefore flood hazard) driven
566 by the nodal cycle at the three Gulf of Maine sites has historically been larger than non-
567 stationarity driven by the ~ 100 -year average rate of SLR (black triangles versus asterisks in Fig.
568 6). In the future, even as SLR accelerates to equal or exceed rates of $ST_{0.01}$ nodal forcing, the
569 nodal cycle will continue to force significant decadal-scale variability in the rate that flood
570 hazard will increase. We illustrate this effect through 2100 by adding the $ST_{0.01}$ nodal forcing
571 rate to the projected mean rate of SLR over 9.3-year periods when nodal forcing will be trending
572 positively (i.e. moving from a minimum toward a maximum). Over 9.3-year periods when the
573 nodal cycle will be trending negatively, we subtract nodal forcing from projected SLR. We use
574 Kopp et al. (2014) probabilistic local SLR projections, but we modify the ice sheet contributions
575 by replacing the Church et al. (2013) likely ranges with Oppenheimer et al. (2019) likely ranges.

576 The nodal cycle is currently in its negative phase in the Gulf, and until it reaches its
577 minimum in 2025, negative nodal forcing will counteract the SLR-induced increase in flood
578 hazard. Between 2025 and 2034 (and in all decades when the nodal cycle is moving from a
579 minimum to a maximum), however, positive nodal forcing will accelerate the flood hazard
580 increase. Thus, it is critical to consider SLR and nodal cycle forcing together in planning for the
581 transition to chronic flooding that will be driven by SLR in many coastal regions over the next
582 century (e.g. Ray & Foster, 2016; Buchanan et al., 2017; Kopp et al., 2017; Talke et al., 2018;
583 Oppenheimer et al., 2019).

584 4.5 Limitations

585 We demonstrate that the qn-SSJPM provides more precise and stable storm tide
586 exceedance estimates than the commonly used GPD fit to measured storm tides. However, there
587 are sources of uncertainty in the method, and there are additional forcings of interannual storm
588 tide variation that we do not account for. The skew surge GPD is a significant source of
589 uncertainty, as GPD parameters are sensitive to both the choice of threshold (e.g. Coles, 2001;
590 Arns et al., 2013) and the largest observed skew surge values (e.g. Tawn and Vassie, 1989;
591 Tawn, 1992; Haigh et al., 2010). We show that the qn-SSJPM is stable against a range of skew
592 surge GPD thresholds for Boston through the 0.002 exceedances/year level (Fig. 4), and this
593 should always be tested. Furthermore, the accuracy of skew surge values depends on the
594 accuracy of tidal predictions. The `r_t_tide` software does not include minor constituents (for
595 example, our Boston `r_t_tide` predictions use 67 constituents, compared to the 108 used by Ray
596 and Foster, 2016), and our calculations do not include tide prediction errors. The errors,
597 however, are small; for example, M_2 amplitude errors are on the order of 0.1% (~ 0.001 – 0.003
598 meters).

599 The qn-SSJPM also does not incorporate climatic variability that may impact storm tide
600 hazard relative to annual MSL. For example, the North Atlantic Oscillation drives interannual
601 variation in New England sea levels via northeasterly wind stress anomalies on the upper ocean
602 (Goddard et al., 2015). In the future, increasing sea surface temperatures and changing
603 atmospheric circulation patterns may also drive changes in storm intensity and frequency, but
604 there is low confidence in site-specific projections of future storm behavior (e.g. Knutson et al.,
605 2010; Emanuel et al., 2013), making it difficult to incorporate storm non-stationarity into flood
606 hazard assessment.

607 Finally, the qn-SSJPM does not consider the impact of wave processes on flood hazard
608 and is therefore most suitable for wave-sheltered harbors and embayments. During flood events,

609 wave set-up elevates the time-averaged water level, and wave run-up periodically further raises
610 water level (Stockdon et al., 2006; O’Grady et al., 2019). These processes must be included for
611 hazard analyses to be reliable at wave-exposed coastlines; for example, Lambert et al. (2020)
612 demonstrate that neglecting waves can lead to overestimating the time it will take for sea-level
613 rise to double the frequency of a given extreme water level. Furthermore, our analysis does not
614 explicitly account for water level oscillations just below wind-wave frequencies in the
615 infragravity spectrum, generally defined between 0.04 and 0.004 Hz (Bertin et al., 2018).
616 Infragravity waves are not only an important component of wave-induced run-up along open
617 coasts (Stockdon et al., 2006), but can also contribute to flooding in harbors, particularly when
618 amplified by resonance (e.g. Rabinovich, 2010; Bertin et al., 2015).

619 **5 Conclusions**

620 We present a new quasi-nonstationary skew surge joint probability method for
621 calculating storm tide exceedances and apply it along the Gulf of Maine coast, where tides are
622 large and vary year-to-year. In addition to providing separate statistical treatment of tides and
623 surge, the qn-SSJPM calculates distinct annual storm tide exceedance curves that account for
624 interannual variation in tides. Each year’s curve is a convolution of 1) predicted high water
625 probabilities, which are known based on that year’s tide predictions, and 2) skew surge
626 probabilities determined from a GPD fit to all skew surges recorded over the length of a tide
627 gauge record.

628 We use a Monte Carlo validation and a GPD threshold sensitivity test to compare the qn-
629 SSJPM to the commonly used method of fitting a GPD to times series of measured storm tides.
630 We find that the qn-SSJPM provides more precise and stable storm tide frequency estimates
631 because it is less susceptible to being biased by the largest few events within the observational
632 period, and it is more stable with respect to GPD threshold selection. We also show that in
633 Boston, qn-SSJPM-derived storm tide frequency estimates based on the 100-year NOAA record
634 match those based on the extended, 200-year Talke et al. (2018) record.

635 At all three Gulf of Maine sites, we find that interannual variation in tides significantly
636 impacts design-relevant flood levels, such as winter storm tides at the 0.01 exceedances/year
637 level ($ST_{0.01}$). The 18.6-year nodal cycle forces decadal oscillations in $ST_{0.01}$ at a rate of 13.5
638 mm/year in Eastport, 4.0 mm/year in Portland, and 5.9 mm/year in Boston. In comparison, the
639 average historical rate of local SLR over the past century has been between 1.89 and 2.86
640 mm/year at the three sites. Nodal forcing is currently counteracting the SLR-induced increase in
641 flood hazard; however, in 2025, the nodal cycle will reach a minimum and then begin
642 accelerating flood hazard increase as it moves toward its maximum phase over the subsequent
643 decade.

644 SLR is driving a transition to severe chronic flooding in many coastal regions (e.g.
645 Oppenheimer et al., 2019). Flooding becomes severe when water elevations cross thresholds
646 defined by local topography and flood defense structures, and the nodal cycle entering a positive
647 phase may drive flood heights above these thresholds sooner than SLR would alone. Thus,
648 considering tidal non-stationarity and SLR together is key to long-term municipal planning and
649 emergency management along meso-to-macrotidal coastlines.

650 **Acknowledgments and Data**

651 H.E.B. was supported by the National Aeronautics and Space Administration (Award
652 NNX16AO24H). We thank two anonymous reviewers whose comments improved the

653 manuscript. Datasets for this research are available in these in-text citation references: Caldwell
654 et al. (2010), Talke et al. (2018), and <https://tidesandcurrents.noaa.gov>. All of the code we used
655 to produce results is available at <https://doi.org/10.5281/zenodo.3898659> with a Creative
656 Commons Attribution 4.0 International license.

657 **References**

- 658 Arns, A., Wahl, T., Haigh, I. D., Jensen, J., & Pattiaratchi, C. (2013). Estimating extreme water
659 level probabilities: A comparison of the direct methods and recommendations for best
660 practise. *Coastal Engineering*, *81*, 51–66. <https://doi.org/10.1016/j.coastaleng.2013.07.003>
- 661 Batstone, C., Lawless, M., Tawn, J., Horsburgh, K., Blackman, D., McMillan, A., Worth, D.,
662 Laeger, S., & Hunt, T. (2013). A UK best-practice approach for extreme sea-level analysis
663 along complex topographic coastlines. *Ocean Engineering*, *71*, 28–39.
664 <https://doi.org/10.1016/j.oceaneng.2013.02.003>
- 665 Bertin, X., de Bakker, A., van Dongeren, A., Coco, G., André, G., Ardhuin, F., et al. (2018).
666 Infragravity waves: From driving mechanisms to impacts. *Earth-Science Reviews*, *177*,
667 774–799. <https://doi.org/10.1016/j.earscirev.2018.01.002>
- 668 Buchanan, M. K., Kopp, R. E., Oppenheimer, M., & Tebaldi, C. (2016). Allowances for evolving
669 coastal flood risk under uncertain local sea-level rise. *Climatic Change*, *137*(3), 347–362.
670 <https://doi.org/10.1007/s10584-016-1664-7>
- 671 Buchanan, M. K., Oppenheimer, M., & Kopp, R. E. (2017). Amplification of flood frequencies
672 with local sea level rise and emerging flood regimes. *Environmental Research Letters*,
673 *12*(6), 064009. <https://doi.org/10.1088/1748-9326/aa6cb3>
- 674 Caldwell, P. C., Merrifield, M. A., & Thompson, P. R. (2010). *Sea level measured by tide gauges*
675 *from global oceans as part of the Joint Archive for Sea Level (JASL) since 1846* [Data set].
676 National Oceanographic Data Center, NOAA. <https://doi.org/10.7289/V5V40S7W>
- 677 Church, J. A., Clark, P. U., Cazenave, A., Gregory, J. M., Jevrejeva, S., Levermann, A.,
678 Merrifield, M. A., Milne, G. A., Nerem, R. S., Nunn, P. D., Payne, A. J., Pfeffer, W. T.,
679 Stammer, D., & Unnikrishnan, A. S. (2013). *Sea level change* [Technical Report].
680 P.M. Cambridge University Press. <http://drs.nio.org/drs/handle/2264/4605>
- 681 Coles, S. (2001). *An Introduction to Statistical Modeling of Extreme Values*. Springer.
- 682 Dodet, G., Melet, A., Ardhuin, F., Bertin, X., Idier, D., & Almar, R. (2019). The Contribution of
683 Wind-Generated Waves to Coastal Sea-Level Changes. *Surveys in Geophysics*, *40*(6),
684 1563–1601. <https://doi.org/10.1007/s10712-019-09557-5>
- 685 Douglas, E., Kirshen, P., DeConto, R. M., FitzGerald, D. M., Hay, C., Hughes, Z., Kemp, A. C.,
686 Kopp, R. E., Anderson, B., Kuang, Z., Ravela, S., Woodruff, J. D., Barlow, M., Collins, M.,
687 DeGaetano, A., Schlosser, C. A., Ganguly, A., Kodra, E., & Ruth, M. (2016). *Climate*
688 *change and sea level rise projections for Boston: The Boston Research Advisory Group*

- 689 *report.* (p. 54). Climate Ready Boston.
690 https://www.boston.gov/sites/default/files/document-file-12-2016/brag_report_-_final.pdf
- 691 Eliot, M. (2010). Influence of interannual tidal modulation on coastal flooding along the Western
692 Australian coast. *Journal of Geophysical Research: Oceans*, *115*(C11).
693 <https://doi.org/10.1029/2010JC006306>
- 694 Emanuel, K. A. (2013). Downscaling CMIP5 climate models shows increased tropical cyclone
695 activity over the 21st century. *Proceedings of the National Academy of Sciences*, *110*(30),
696 12219–12224. <https://doi.org/10.1073/pnas.1301293110>
- 697 Familkhalili, R., Talke, S. A., & Jay, D. A. (n.d.). Tide-Storm Surge Interactions in Highly
698 Altered Estuaries: How Channel Deepening Increases Surge Vulnerability. *Journal of*
699 *Geophysical Research: Oceans*, *n/a*(n/a), e2019JC015286.
700 <https://doi.org/10.1029/2019JC015286>
- 701 Ferro, C. A. T., & Segers, J. (2003). Inference for clusters of extreme values. *Journal of the*
702 *Royal Statistical Society: Series B (Statistical Methodology)*, *65*(2), 545–556.
703 <https://doi.org/10.1111/1467-9868.00401>
- 704 Galloway, G. E., Baecher, G. B., Plasencia, D., Coulton, K. G., Louthain, J., Bagha, M., & Levy,
705 A. R. (2006). *Assessing the Adequacy of the National Flood Insurance Program's 1 Percent*
706 *Flood Standard* (p. 197) [2001-2006 Evaluation of the National Flood Insurance Program].
707 [http://s3-us-gov-west-1.amazonaws.com/dam-production/uploads/20130726-1602-20490-](http://s3-us-gov-west-1.amazonaws.com/dam-production/uploads/20130726-1602-20490-6095/nfip_eval_1_percent_standard.pdf)
708 [6095/nfip_eval_1_percent_standard.pdf](http://s3-us-gov-west-1.amazonaws.com/dam-production/uploads/20130726-1602-20490-6095/nfip_eval_1_percent_standard.pdf)
- 709 Garner, A. J., Mann, M. E., Emanuel, K. A., Kopp, R. E., Lin, N., Alley, R. B., Horton, B. J.,
710 DeConto, R. M., Donnelly, J. P., & Pollard, D. (2017). Impact of climate change on New
711 York City's coastal flood hazard: Increasing flood heights from the preindustrial to 2300
712 CE. *Proceedings of the National Academy of Sciences*, *114*(45), 11861–11866.
713 <https://doi.org/10.1073/pnas.1703568114>
- 714 Garrett, C. (1972). Tidal Resonance in the Bay of Fundy and Gulf of Maine. *Nature*, *238*(5365),
715 441–443. <https://doi.org/10.1038/238441a0>
- 716 Goddard, P. B., Yin, J., Griffies, S. M., & Zhang, S. (2015). An extreme event of sea-level rise
717 along the Northeast coast of North America in 2009–2010. *Nature Communications*, *6*(1),
718 1–9. <https://doi.org/10.1038/ncomms7346>
- 719 Godin, G. (1993). On tidal resonance. *Continental Shelf Research*, *13*(1), 89–107.
720 [https://doi.org/10.1016/0278-4343\(93\)90037-X](https://doi.org/10.1016/0278-4343(93)90037-X)
- 721 Greenberg, D. A., Blanchard, W., Smith, B., & Barrow, E. (2012). Climate Change, Mean Sea
722 Level and High Tides in the Bay of Fundy. *Atmosphere-Ocean*, *50*(3), 261–276.
723 <https://doi.org/10.1080/07055900.2012.668670>
- 724 Griggs, G., Arvai, J., Cayan, D., DeConto, R. M., Fox, J., Fricker, H. A., Kopp, R. E., Tebaldi,
725 C., & Whiteman, E. A. (2017). *Rising seas in California: An update on sea-level rise*

- 726 *science*. (p. 71) [California Ocean Science Trust Tech. Rep.].
727 <http://climate.calcommons.org/bib/rising-seas-california-update-sea-level-rise-science>
- 728 Haigh, I. D., Eliot, M., & Pattiaratchi, C. (2011). Global influences of the 18.61 year nodal cycle
729 and 8.85 year cycle of lunar perigee on high tidal levels. *Journal of Geophysical Research:*
730 *Oceans*, 116(C6). <https://doi.org/10.1029/2010JC006645>
- 731 Haigh, I. D., Nicholls, R., & Wells, N. (2010). A comparison of the main methods for estimating
732 probabilities of extreme still water levels. *Coastal Engineering*, 57(9), 838–849.
733 <https://doi.org/10.1016/j.coastaleng.2010.04.002>
- 734 Haigh, I. D., Pickering, M. D., Green, J. A. M., Arbic, B. K., Arns, A., Dangendorf, S., Hill, D.
735 F., Horsburgh, K., Howard, T., Idier, D., Jay, D. A., Jänicke, L., Lee, S. B., Müller, M.,
736 Schindelegger, M., Talke, S. A., Wilmes, S.-B., & Woodworth, P. L. (2020). The Tides
737 They Are A-Changin': A Comprehensive Review of Past and Future Nonastronomical
738 Changes in Tides, Their Driving Mechanisms, and Future Implications. *Reviews of*
739 *Geophysics*, 58(1), e2018RG000636. <https://doi.org/10.1029/2018RG000636>
- 740 Hallegatte, S., Green, C., Nicholls, R. J., & Corfee-Morlot, J. (2013). Future flood losses in
741 major coastal cities. *Nature Climate Change*, 3(9), 802–806.
742 <https://doi.org/10.1038/nclimate1979>
- 743 Horsburgh, K. J., Williams, J. A., Flowerdew, J., & Mylne, K. (2008). Aspects of operational
744 forecast model skill during an extreme storm surge event. *Journal of Flood Risk*
745 *Management*, 1(4), 213–221. <https://doi.org/10.1111/j.1753-318X.2008.00020.x>
- 746 Hunter, J. (2010). Estimating sea-level extremes under conditions of uncertain sea-level rise.
747 *Climatic Change*, 99(3), 331–350. <https://doi.org/10.1007/s10584-009-9671-6>
- 748 Kendall, M. G. (1938). A New Measure of Rank Correlation. *Biometrika*, 30(1/2), 81–93.
749 JSTOR. <https://doi.org/10.2307/2332226>
- 750 Kirshen, P., Knee, K., & Ruth, M. (2008). Climate change and coastal flooding in Metro Boston:
751 Impacts and adaptation strategies. *Climatic Change*, 90(4), 453–473.
752 <https://doi.org/10.1007/s10584-008-9398-9>
- 753 Knutson, T. R., McBride, J. L., Chan, J., Emanuel, K., Holland, G., Landsea, C., Held, I., Kossin,
754 J. P., Srivastava, A. K., & Sugi, M. (2010). Tropical cyclones and climate change. *Nature*
755 *Geoscience*, 3(3), 157–163. <https://doi.org/10.1038/ngeo779>
- 756 Kopp, R. E., Horton, R. M., Little, C. M., Mitrovica, J. X., Oppenheimer, M., Rasmussen, D. J.,
757 Strauss, B. H., & Tebaldi, C. (2014). Probabilistic 21st and 22nd century sea-level
758 projections at a global network of tide-gauge sites. *Earth's Future*, 2(8), 383–406.
759 <https://doi.org/10.1002/2014EF000239>
- 760 Ku, L.-F., Greenberg, D. A., Garrett, C. J. R., & Dobson, F. W. (1985). Nodal Modulation of the
761 Lunar Semidiurnal Tide in the Bay of Fundy and Gulf of Maine. *Science*, 230(4721), 69–
762 71. <https://doi.org/10.1126/science.230.4721.69>

- 763 Lambert, E., Rohmer, J., Cozannet, G. L., & Wal, R. S. W. van de. (2020). Adaptation time to
764 magnified flood hazards underestimated when derived from tide gauge records.
765 *Environmental Research Letters*. <https://doi.org/10.1088/1748-9326/ab8336>
- 766 Leadbetter, M. R. (1983). Extremes and local dependence in stationary sequences. *Zeitschrift*
767 *Für Wahrscheinlichkeitstheorie Und Verwandte Gebiete*, 65(2), 291–306.
768 <https://doi.org/10.1007/BF00532484>
- 769 Leffler, K., & Jay, D. A. (2009). Enhancing tidal harmonic analysis: Robust (hybrid L1/L2)
770 solutions. *Continental Shelf Research*, 29(1), 78–88.
771 <https://doi.org/10.1016/j.csr.2008.04.011>
- 772 Lin, N., Emanuel, K. A., Smith, J. A., & Vanmarcke, E. (2010). Risk assessment of hurricane
773 storm surge for New York City. *Journal of Geophysical Research: Atmospheres*, 115(D18).
774 <https://doi.org/10.1029/2009JD013630>
- 775 Melet, A., Meyssignac, B., Almar, R., & Le Cozannet, G. (2018). Under-estimated wave
776 contribution to coastal sea-level rise. *Nature Climate Change*, 8(3), 234–239.
777 <https://doi.org/10.1038/s41558-018-0088-y>
- 778 Menéndez, M., & Woodworth, P. L. (2010). Changes in extreme high water levels based on a
779 quasi-global tide-gauge data set. *Journal of Geophysical Research: Oceans*, 115(C10).
780 <https://doi.org/10.1029/2009JC005997>
- 781 Müller, M., Arbic, B. K., & Mitrovica, J. X. (2011). Secular trends in ocean tides: Observations
782 and model results. *Journal of Geophysical Research: Oceans*, 116(C5).
783 <https://doi.org/10.1029/2010JC006387>
- 784 Müller, M. (2012). The influence of changing stratification conditions on barotropic tidal
785 transport and its implications for seasonal and secular changes of tides. *Continental Shelf*
786 *Research*, 47, 107–118. <https://doi.org/10.1016/j.csr.2012.07.003>
- 787 National Environment Research Council (1975). *The Flood Studies Report*. London: Natural
788 Environment Research Council.
- 789 Neumann, B., Vafeidis, A. T., Zimmermann, J., & Nicholls, R. J. (2015). Future Coastal
790 Population Growth and Exposure to Sea-Level Rise and Coastal Flooding—A Global
791 Assessment. *PLOS ONE*, 10(3), e0118571. <https://doi.org/10.1371/journal.pone.0118571>
- 792 NYC. (2013). *A stronger, more resilient New York* (p. 435) [New York City PlaNYC Tech
793 Rep.].
794 https://www1.nyc.gov/assets/sirr/downloads/pdf/Ch_2_ClimateAnalysis_FINAL_singles.pdf
795 f
- 796 Oppenheimer, M., Glavovic, B. C., Hinkel, J., van de Wal, R., Magnan, A. K., Abd-Elgawad, A.,
797 Cai, R., Cifuentes-Jara, M., DeConto, R. M., Ghosh, T., Hay, J., Isla, F., Marzeion, B.,
798 Meyssignac, B., & Sebesvari, Z. (n.d.). *Sea Level Rise and Implications for Low-Lying*

799 *Islands, Coasts and Communities*. (IPCC Special Report on the Ocean and Cryosphere in a
800 Changing Climate).

801 Pawlowicz, R., Beardsley, B., & Lentz, S. (2002). Classical tidal harmonic analysis including
802 error estimates in MATLAB using T_TIDE. *Computers & Geosciences*, 28(8), 929–937.
803 [https://doi.org/10.1016/S0098-3004\(02\)00013-4](https://doi.org/10.1016/S0098-3004(02)00013-4)

804 Pelling, H. E., & Green, J. A. M. (2013). Sea level rise and tidal power plants in the Gulf of
805 Maine. *Journal of Geophysical Research: Oceans*, 118(6), 2863–2873.
806 <https://doi.org/10.1002/jgrc.20221>

807 Peng, D., Hill, E. M., Meltzner, A. J., & Switzer, A. D. (2019). Tide Gauge Records Show That
808 the 18.61-Year Nodal Tidal Cycle Can Change High Water Levels by up to 30 cm. *Journal*
809 *of Geophysical Research: Oceans*, 124(1), 736–749. <https://doi.org/10.1029/2018JC014695>

810 Pugh D. T., & Vassie J. M. (1978). Extreme Sea Levels from Tide and Surge Probability.
811 *Coastal Engineering 1978*, 911–930. <https://doi.org/10.1061/9780872621909.054>

812 Pugh, D., & Vassie, J. (1980). Applications of the joint probability method for extreme sea level
813 computations. *Proceedings of the Institution of Civil Engineers*, 69(4), 959–975.
814 <https://doi.org/10.1680/iicep.1980.2179>

815 Rabinovich, A. B. (2009). Seiches and Harbor Oscillations. In: *Handbook of Coastal and Ocean*
816 *Engineering* (Vol. 1–0, pp. 193–236). WORLD SCIENTIFIC.
817 https://doi.org/10.1142/9789812819307_0009

818 Ray, R. D. (2006). Secular changes of the M2 tide in the Gulf of Maine. *Continental Shelf*
819 *Research*, 26(3), 422–427. <https://doi.org/10.1016/j.csr.2005.12.005>

820 Ray, R. D., & Merrifield, M. A. (2019). The Semiannual and 4.4-Year Modulations of Extreme
821 High Tides. *Journal of Geophysical Research: Oceans*, 124(8), 5907–5922.
822 <https://doi.org/10.1029/2019JC015061>

823 Ray, R. D., & Talke, S. A. (2019). Nineteenth-Century Tides in the Gulf of Maine and
824 Implications for Secular Trends. *Journal of Geophysical Research: Oceans*, 124(10), 7046–
825 7067. <https://doi.org/10.1029/2019JC015277>

826 Ray, Richard D., & Foster, G. (2016). Future nuisance flooding at Boston caused by
827 astronomical tides alone. *Earth's Future*, 4(12), 578–587.
828 <https://doi.org/10.1002/2016EF000423>

829 Schindelegger, M., Green, J. a. M., Wilmes, S.-B., & Haigh, I. D. (2018). Can We Model the
830 Effect of Observed Sea Level Rise on Tides? *Journal of Geophysical Research: Oceans*,
831 123(7), 4593–4609. <https://doi.org/10.1029/2018JC013959>

832 Sobey, R. J. (2005). Extreme low and high water levels. *Coastal Engineering*, 52(1), 63–77.
833 <https://doi.org/10.1016/j.coastaleng.2004.09.003>

- 834 Talke, S. A., Kemp, A. C., & Woodruff, J. (2018). Relative Sea Level, Tides, and Extreme Water
835 Levels in Boston Harbor From 1825 to 2018. *Journal of Geophysical Research: Oceans*,
836 123(6), 3895–3914. <https://doi.org/10.1029/2017JC013645>
- 837 Talke, S. A., Mahedy, A., Jay, D. A., Lau, P., Hilley, C., & Hudson, A. (2020). Sea Level, Tidal,
838 and River Flow Trends in the Lower Columbia River Estuary, 1853–present. *Journal of*
839 *Geophysical Research: Oceans*, 125(3), e2019JC015656.
840 <https://doi.org/10.1029/2019JC015656>
- 841 Talke, Stefan A, & Jay, D. A. (2020). Changing Tides: The Role of Natural and Anthropogenic
842 Factors. *Annual Review of Marine Science*, 12, 121–151. [https://doi.org/10.1146/annurev-](https://doi.org/10.1146/annurev-marine-010419-010727)
843 [marine-010419-010727](https://doi.org/10.1146/annurev-marine-010419-010727)
- 844 Tawn, J. A., & Vassie, J. M. (1989). *Extreme Sea Levels: the Joint Probabilities Method*
845 *Revisited and Revised*. <https://trid.trb.org/view/435293>
- 846 Tawn, Jonathan A. (1992). Estimating Probabilities of Extreme Sea-Levels. *Journal of the Royal*
847 *Statistical Society: Series C (Applied Statistics)*, 41(1), 77–93.
848 <https://doi.org/10.2307/2347619>
- 849 Tebaldi, C., Strauss, B. H., & Zervas, C. E. (2012). Modelling sea level rise impacts on storm
850 surges along US coasts. *Environmental Research Letters*, 7(1), 014032.
851 <https://doi.org/10.1088/1748-9326/7/1/014032>
- 852 Thompson, P. R., Mitchum, G. T., Vonesch, C., & Li, J. (2013). Variability of Winter
853 Storminess in the Eastern United States during the Twentieth Century from Tide Gauges.
854 *Journal of Climate*, 26(23), 9713–9726. <https://doi.org/10.1175/JCLI-D-12-00561.1>
- 855 Vousdoukas, M. I., Voukouvalas, E., Mentaschi, L., Dottori, F., Giardino, A., Bouziotas, D.,
856 Bianchi, A., Salamon, P., & Feyen, L. (2016). Developments in large-scale coastal flood
857 hazard mapping. *Natural Hazards and Earth System Sciences*, 16(8), 1841–1853.
858 <https://doi.org/10.5194/nhess-16-1841-2016>
- 859 Wahl, T., Haigh, I. D., Nicholls, R. J., Arns, A., Dangendorf, S., Hinkel, J., & Slangen, A. B. A.
860 (2017). Understanding extreme sea levels for broad-scale coastal impact and adaptation
861 analysis. *Nature Communications*, 8(1), 1–12. <https://doi.org/10.1038/ncomms16075>
- 862 Wahl, Thomas, & Chambers, D. P. (2015). Evidence for multidecadal variability in US extreme
863 sea level records. *Journal of Geophysical Research: Oceans*, 120(3), 1527–1544.
864 <https://doi.org/10.1002/2014JC010443>
- 865 Williams, J., Horsburgh, K. J., Williams, J. A., & Proctor, R. N. F. (2016). Tide and skew surge
866 independence: New insights for flood risk. *Geophysical Research Letters*, 43(12), 6410–
867 6417. <https://doi.org/10.1002/2016GL069522>
- 868 Winterwerp, J. C., Wang, Z. B., van Braeckel, A., van Holland, G., & Kösters, F. (2013). Man-
869 induced regime shifts in small estuaries—II: A comparison of rivers. *Ocean Dynamics*,
870 63(11), 1293–1306. <https://doi.org/10.1007/s10236-013-0663-8>

871 Woodworth, P. L. (2010). A survey of recent changes in the main components of the ocean tide.
872 *Continental Shelf Research*, 30(15), 1680–1691. <https://doi.org/10.1016/j.csr.2010.07.002>

873 Woodworth, P. L., Melet, A., Marcos, M., Ray, R. D., Wöppelmann, G., Sasaki, Y. N., Cirano,
874 M., Hibbert, A., Huthnance, J. M., Monserrat, S., & Merrifield, M. A. (2019). Forcing
875 Factors Affecting Sea Level Changes at the Coast. *Surveys in Geophysics*, 40(6), 1351–
876 1397. <https://doi.org/10.1007/s10712-019-09531-1>

877 Zervas, C. (2013). *Extreme Water Levels of the United States 1893-2010* (NOAA Technical
878 Report NOS CO-OPS 067; p. 200). NOAA.
879 [https://tidesandcurrents.noaa.gov/publications/NOAA_Technical_Report_NOS_COOPS_06](https://tidesandcurrents.noaa.gov/publications/NOAA_Technical_Report_NOS_COOPS_067a.pdf)
880 [7a.pdf](https://tidesandcurrents.noaa.gov/publications/NOAA_Technical_Report_NOS_COOPS_067a.pdf)

881

882 **Table S1.** Results of Kendall's tau correlation test, using the top 1% of skew surges and their
 883 associated predicted high waters.

	Summer		Winter	
	tau	p-value	tau	p-value
Eastport	0.02	0.59	-0.02	0.58
Portland	-0.01	0.80	-0.08	0.03
Boston	0.05	0.14	0.01	0.75

884

885 **Table S2.** Threshold values and number of observations included in threshold sensitivity test
 886 (see Fig. 4 in main text).

Threshold percentile	Skew GPD (qn-SSJPM)		Storm tide GPD (GPD _{ST})	
	Threshold (m)	# Values above threshold	Threshold (m)	# Values above threshold
99.5	0.57	170	2.25	155
99.6	0.60	134	2.28	128
99.7	0.63	101	2.31	94
99.8	0.68	69	2.35	60
99.9	0.77	33	2.44	32

887